

## Accurate viscoelastic modeling by frequency-domain finite differences using rotated operators

I. Štekl\* and R. G. Pratt†

### ABSTRACT

The viscoelastic wave equation is an integro-differential equation that requires special methods when using time-domain numerical finite-difference methods. In the frequency domain, the integral terms are easily represented by complex valued elastic media properties. There are further significant advantages to using the frequency domain if the forward or the inverse problem requires modeling or inverting a large number of prestack source gathers.

Numerical modeling is expensive for seismic data because of the large number of wavelengths typically separating sources from receivers, which results in a need for a large number of grid points. A major obstacle to using frequency-domain methods is the consequent storage requirements. To reduce these, we maximize the accuracy and simultaneously minimize the spatial extent of the numerical operators. We achieve this by extending earlier published methods introduced for the viscoacoustic case to the viscoelastic case. This requires the formulation of two new numerical operators: a differencing operator in a rotated coordinate frame and a lumped mass term.

The new operators are combined with ordinary second-order, finite-difference operators in an optimal manner to minimize numerical errors without increasing the size of the numerical operator.

For a fixed number of grid points, the resulting second-order differencing scheme is no more expensive than an ordinary second-order differencing scheme, but a numerical dispersion analysis shows that the number of grid points required per smallest wavelength is reduced from approximately 15 to approximately 4. The new scheme is also capable of handling embedded fluid layers without instability. We demonstrate that no further improvement in performance can be achieved using higher order spatial operators because of the associated computational overheads associated with the larger differencing operators.

The new viscoelastic modeling scheme is used to study a crosshole data set in which the exact nature of the seismic coda is unclear. The results of the modeling study indicate this coda is likely related to the generation of mode-converted shear waves within the complicated, finely layered sediments at the site.

### INTRODUCTION

Modeling the propagation of seismic waves and predicting the response at seismic receivers is an essential step in the interpretation or, formally, inversion of data from seismic experiments. To model complete wide-band seismic wave behavior in a heterogeneous viscoelastic medium, numerical modeling of the full viscoelastic wave equation is required. Ideally, one would like to include, if possible, three dimensions (3-D), general anisotropy, and arbitrary viscoelasticity. While formulations for 3-D anisotropic media are possible (Mora, 1989; Carcione et al., 1992), the memory and time requirements for

realistic model sizes still prevent the production usage of such methods. Instead there has been a historical progression toward the practical use of more general methods (Alterman and Karal, 1968; Kelly et al., 1976; Gazdag, 1981; Dablain, 1986; Virieux, 1986; Holdberg, 1987; Dai et al., 1995).

The advantage of using a particular numerical method depends on the complexity of the model. For simple models the boundary integral method (Dravinski, 1973; Schuster, 1984; Campillo and Bouchon, 1985; Bouchon et al., 1989) can be optimal, while for fully heterogeneous models finite-difference methods or finite-element methods (Drake, 1972; Smith, 1974; Marfurt, 1984b) are better suited. In practice, rectangular grids

Manuscript received by the Editor October 15, 1996; revised manuscript received August 25, 1997.

\*Department of Geology, Imperial College of Science, Technology and Medicine, London SW7 2BP, United Kingdom; E-mail: i.stekl@ic.ac.uk.

†Formerly Department of Geology, Imperial College of Science, Technology and Medicine, London SW7 2BP, United Kingdom; presently Queen's University, Kingston, Ontario K7L 3N6, Canada; E-mail: pratt@geol.queensu.ca.

© 1998 Society of Exploration Geophysicists. All rights reserved.

Reprinted from Geophysics, 63, 1779–1794. © 1998 Society of Exploration Geophysicists

(or more commonly square grids) are often used, in which case the finite-difference method and the finite-element method are closely related (Marfurt, 1984a).

Recently, much attention has been focused on the modeling of seismic waves in models that include viscoelastic losses (Emmerich and Korn, 1987; Carcione et al., 1988; Robertsson et al., 1994; Carcione, 1995). If viscoelastic losses are related to time-dependent creep and relaxation effects (see, for example, Kjartansson, 1979), this leads to integral terms in the wave equation, which require special techniques when modeling using time-domain methods.

A solution to the difficulty of representing integral terms in the time-dependent wave equation is to transform the equations into the frequency domain and model the resultant Helmholtz-type equations. This allows frequency-dependent attenuation to be represented easily by complex valued elastic parameters (Müller, 1983). By fortunate coincidence, there are computational advantages to the frequency-domain methods when compared with time-domain techniques. These advantages—pointed out by Marfurt (1984b) and utilized by Pratt (1989), Pratt and Goult (1991), and Song et al. (1995)—are realized when the complete prestack seismic response is required for a multiple-source experiment or if a formal inversion of the prestack seismic data is under consideration (as in Song et al., 1995, and Pratt et al., 1995).

The numerical considerations associated with frequency-domain forward modeling are profoundly different from those encountered with time-domain methods: Once the frequency-domain equations are discretized, the solution (at a given frequency) is implicit in the solution of an extremely large matrix equation. The essential problem is to minimize the memory required to store the matrix. When solving such matrix equations, a key parameter is the numerical bandwidth, a measure of the distribution of the nonzero matrix elements away from the main diagonal. Second-order differencing with standard ordering schemes leads to well-structured band diagonal matrices. Elements outside the band diagonal structure need not be stored because they remain zero valued as the solution scheme proceeds (Press et al., 1992). More complex solution schemes attempt to minimize the numerical bandwidth by reordering the matrix elements. The numerical bandwidth is ultimately controlled by the spatial extent of the differencing operators, which consequently must be kept as small and as accurate as possible.

This paper describes the method we have developed and implemented to improve the accuracy and efficiency of 2-D isotropic, frequency-domain viscoelastic seismic modeling. Our scheme uses the same grid points in the computational star as a standard second-order differencing scheme, thus conserving numerical bandwidth. It allows a significant reduction in the size of the numerical mesh (from approximately 15 grid points per smallest wavelength in the model to approximately 4 grid points per wavelength), dramatically reducing computational costs. We also show that no further reduction in cost can be achieved by using a larger computational star, no matter how accurate.

In essence, our new scheme is the extension to the viscoelastic case of an idea introduced by Jo et al. (1996) for viscoacoustic modeling, itself an extension of ideas introduced earlier by Cole (1994) (Cole's work is in the time domain). The method of Jo et al. (1996) introduces two new numerical operators,

the first in a rotated coordinate frame and the second using a lumped mass term, both of which are combined with standard second-order numerical operators in an optimal manner to minimize numerical errors.

Our paper begins with a development of the required differencing operators. Because the viscoelastic wavefield (i.e., the displacement) is a vector quantity, the rotation of the coordinate frame presents additional difficulties (when compared with the viscoacoustic case). Moreover, since the 2-D differencing operators are nine-point stars (as opposed to the five-point stars required for acoustic modeling), the rotated operators must be modified to minimize their spatial extent. We show how the required rotation can be achieved on the original nine-point star. The second modification introduced by Jo et al. (1996), the use of a lumped mass term, is dealt with in a straightforward manner.

Following the development of the required operators, we then show how the new schemes are to be combined with the original, ordinary second-order operators to yield a scheme that is optimized to have minimum numerical errors. The dispersion analysis required for this optimization is given in Appendix A. We then analyze the numerical errors in the proposed scheme and compare these with the errors for the standard second-order scheme. We also show that, in contrast to the standard second-order scheme, the new scheme correctly predicts a zero numerical shear velocity in fluids. In Appendix B we demonstrate that the nine-point scheme is optimal; no further reduction in cost can be achieved using a larger computational scheme. Finally, we use the modeling scheme to generate synthetic crosshole data from a model representative of the geological section at a near-surface test site. The modeling results demonstrate a possible relationship between strong, late arrivals in these crosshole data and the generation of mode-converted shear waves in the highly layered, attenuating sediments at the site.

## VISCOELASTIC MODELING

In this section we develop fully our method for finite differencing the 2-D, frequency-domain homogeneous elastic wave equation. We will comment at the end of this section on the extension to the heterogeneous wave equation. As with other work in finite-difference methods, we will use the homogeneous formulation to analyze the numerical errors, and we obtain a scheme that minimizes these errors.

The 2-D, second-order, frequency-domain viscoelastic wave equation in a homogeneous, isotropic, and source-free media consists of the two coupled equations

$$\rho\omega^2 u + (\lambda + 2\mu)\frac{\partial^2 u}{\partial x^2} + \mu\frac{\partial^2 u}{\partial z^2} + (\lambda + \mu)\frac{\partial^2 v}{\partial x \partial z} = 0 \quad (1)$$

$$\rho\omega^2 v + (\lambda + 2\mu)\frac{\partial^2 v}{\partial z^2} + \mu\frac{\partial^2 v}{\partial x^2} + (\lambda + \mu)\frac{\partial^2 u}{\partial x \partial z} = 0, \quad (2)$$

where  $\omega = 2\pi f$  is the angular frequency,  $\rho$  is the density, and  $\lambda$  and  $\mu$  are Lamé parameters. To be able to simulate viscoelasticity the Lamé parameters is, in general, frequency dependent and complex valued. The wavefield variables  $u$  and  $v$  are, respectively, the horizontal and vertical components of the Fourier transformed displacements.

### Rotated finite differences: Computational stars

The numerical error of a regular-grid finite-differencing scheme for equations (1) and (2) depends on the wave propagation angle ("numerical anisotropy"). This is because the distance between two discrete grid points is not the same in every direction. Usually, propagation is most accurate in directions parallel to the coordinate axes. The solution suggested by Cole (1994) and Jo et al. (1996) for scalar wave equations is to use two separate coordinate systems, one rotated with respect to the other, on the same discrete numerical mesh. A linear combination of the two results compensates for some of the numerical anisotropy. The linear combination of the results is performed implicitly by the finite-difference scheme. The aim is to minimize the numerical anisotropy yet retain the existing grid and keep the computational star as small as possible.

The basic approach for developing a rotated finite-difference coordinate system is best understood with reference to Figure 1, which depicts the computational differencing stars used to approximate the local partial derivatives on the grid. In the scheme devised by Jo et al. (1996) for acoustic-wave propagation, the five-point difference star for second-order finite differencing of the acoustic wave equation was rotated by  $45^\circ$ , expanded, and overlain on the original grid (see Figure 1a and b). This introduces four additional node points into the star, turning the combined computational star from a five-point star into a nine-point star. For the elastic wave equation, applying standard second-order finite differencing to equations (1) and (2) results in a nine-point computational star (e.g., Pratt, 1989) (Figure 1a). At first sight, it would appear the same technique can be extended to the elastic wave equation by rotating and expanding the computational star, resulting in the new star seen in Figure 1b. Unfortunately, this star dramatically increases the memory requirements and, ultimately, is impractical for forward modeling. To understand this, it is necessary to understand the manner in which the finite-difference approximation of the continuous equations (1) and (2) is actually solved.

In general, wave equations such as (1) and (2) can be represented by

$$\mathcal{L}(\omega)\mathbf{u}(\mathbf{r}) = \mathbf{s}(\mathbf{r}) \quad (3)$$

where  $\mathcal{L}(\omega)$  is the appropriate, frequency-dependent, linear partial differential operator;  $\mathbf{u}(\mathbf{r})$  is the field variable (in this case the displacement, a continuous two-component vector field); and  $\mathbf{s}(\mathbf{r})$  is a source term (zero everywhere except at the location of the source). This equation, together with the boundary conditions, must be satisfied everywhere. In two dimensions, when equation (3) is approximated numerically by finite differences using a grid of  $n \times n$  nodes, this yields the matrix equation

$$\mathbf{F}\mathbf{u} = \mathbf{s}, \quad (4)$$

where  $\mathbf{F}$  is a  $2n^2 \times 2n^2$  complex valued matrix approximating the partial differential operator  $\mathcal{L}(\omega)$ ,  $\mathbf{u}$  is now a  $2n^2$  vector representing the two components of the displacement field at all  $n^2$  node points, and  $\mathbf{s}$  is a similar  $2n^2$  vector representing the source terms.

The matrix  $\mathbf{F}$  represents a significant storage requirement. The requirements are largely determined by the sparsity and the numerical bandwidth of  $\mathbf{F}$  and by the manner in which this structural sparsity is maintained in any solution method. To take advantage of the fact that additional sources involve only a change in the right-side vector,  $\mathbf{s}$ , we use direct solution methods. Direct solvers are also required because, if artificial absorbing boundary conditions are used,  $\mathbf{F}$  will be nonsymmetric and nonpositive definite (precluding iterative solvers that require positive definiteness). It is difficult to formulate direct solvers for arbitrarily sparse matrices; however, it is simple to restrict computations to only those matrix elements that lie within the numerical bandwidth of the matrix. Far better schemes can be developed by making use of optimal ordering schemes; nested dissection (George and Liu, 1981) is such a scheme.

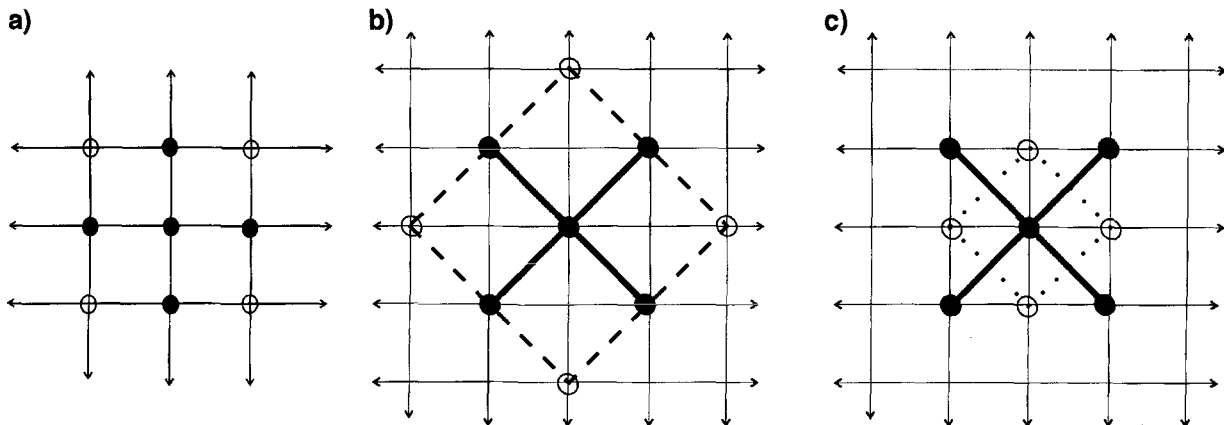


FIG. 1. Computational stars for frequency-domain elastic modeling. These stars indicate the coupling of the central node to the nearest neighbors on the grid. (a) The ordinary, second-order computational star, (b) a possible rotated computational star, and (c) a minimal, rotated computational star. The symbol • represents the coupling of the same displacement components and also represents the only nonzero terms required in acoustic modeling. The symbol ○ represents the coupling between perpendicular displacement components. The star in (c) does not use additional points over the star in view a but introduces additional coupling between components not present in the original star.

The size of the computational star directly determines the sparsity and the numerical bandwidth of the differencing matrix  $\mathbf{F}$ . The bigger the star, the more nonzero elements in the matrix. There is a large computational overhead associated with using a larger differencing star, such as that shown in Figure 1b. The overhead can only be justified if the larger star leads to a greater saving in overhead from increased accuracy. The actual overhead depends strongly on the solution scheme used to solve the matrix equation (we discuss this issue toward the end of the paper). However, it is clear that, if possible, one should minimize the size of the differencing star.

These considerations lead to the new choice of a finite-difference star in the rotated coordinate frame, shown in Figure 1c. This computational star does not require any new grid points. The implication is that there will be no decrease in the sparsity or the numerical bandwidth of the differencing matrix, and the increase in computational cost and storage requirements over the ordinary second-order scheme will be negligible. Having described the design of the optimal differencing star, we now proceed to derive the exact form of the required operators.

### Rotated finite differences: Operators

Solutions to the 2-D, viscoelastic wave equation, represented by the partial differential equations (1) and (2), should naturally be independent of any rotation of the coordinate system in which they are expressed. However, numerical solutions are approximations of the exact solution, and they usually diverge from the actual solution in a manner that depends on the coordinate system. If there is more than one approximate solution for a particular problem, then a linear combination of the solutions may be a more accurate approximate solution for the same problem.

We now introduce a scheme that works with the original Cartesian coordinate system  $(x, z)$  and a new system  $(x', z')$  rotated by  $45^\circ$  (see Figure 1). We assume the equations for both coordinate systems are discretized on the same discretization mesh, with sample intervals  $\Delta_x = \Delta_z \equiv \Delta$ . The relationship between displacements  $u, v$  in the original coordinate system and  $u', v'$  in the new coordinate system is given by

$$u = \frac{1}{\sqrt{2}}(u' - v') \quad v = \frac{1}{\sqrt{2}}(u' + v') \quad (5)$$

and

$$u' = \frac{1}{\sqrt{2}}(u + v) \quad v' = \frac{1}{\sqrt{2}}(v - u). \quad (6)$$

By expressing equations (1) and (2) in the rotated coordinate system, making substitutions (6), and using some simple algebra, we obtain

$$\begin{aligned} \rho\omega^2 u + \frac{1}{2} \left[ (\lambda + 2\mu) \left( \frac{\partial^2 u}{\partial x'^2} - 2 \frac{\partial^2 u}{\partial x' \partial z'} + \frac{\partial^2 u}{\partial z'^2} \right) \right. \\ \left. + \mu \left( \frac{\partial^2 u}{\partial z'^2} + 2 \frac{\partial^2 u}{\partial x' \partial z'} + \frac{\partial^2 u}{\partial x'^2} \right) \right. \\ \left. + (\lambda + \mu) \left( \frac{\partial^2 v}{\partial x'^2} - \frac{\partial^2 v}{\partial z'^2} \right) \right] = 0 \end{aligned} \quad (7)$$

$$\begin{aligned} \rho\omega^2 v + \frac{1}{2} \left[ (\lambda + 2\mu) \left( \frac{\partial^2 v}{\partial x'^2} + 2 \frac{\partial^2 v}{\partial x' \partial z'} + \frac{\partial^2 v}{\partial z'^2} \right) \right. \\ \left. + \mu \left( \frac{\partial^2 v}{\partial z'^2} - 2 \frac{\partial^2 v}{\partial x' \partial z'} + \frac{\partial^2 v}{\partial x'^2} \right) \right. \\ \left. + (\lambda + \mu) \left( \frac{\partial^2 u}{\partial x'^2} - \frac{\partial^2 u}{\partial z'^2} \right) \right] = 0. \end{aligned} \quad (8)$$

This procedure transforms the field variables from the rotated coordinate system into the original coordinate system but leaves the coordinate axes themselves in the rotated frame of reference. This is required to be able to combine the resulting numerical solutions with numerical solutions to the original system.

We now have two partial differential equation systems. In the original coordinate system,

$$\rho\omega^2 u + A_1 = 0 \quad (9)$$

and

$$\rho\omega^2 v + B_1 = 0, \quad (10)$$

where  $A_1$  and  $B_1$  are the partial differential parts of equations (1) and (2). In the new (rotated) coordinate system,

$$\rho\omega^2 u + A_2 = 0 \quad (11)$$

and

$$\rho\omega^2 v + B_2 = 0, \quad (12)$$

where  $A_2$  and  $B_2$  are the partial differential parts of equations (7) and (8). We describe below the differencing operators used to approximate these two systems. The resulting two numerical systems will each have numerical errors, but these errors and the numerical anisotropy for the two systems will differ.

We can write a linear combination of the two systems as

$$\rho\omega^2 u + aA_1 + (1-a)A_2 = 0 \quad (13)$$

and

$$\rho\omega^2 v + aB_1 + (1-a)B_2 = 0; \quad (14)$$

by varying the coefficient  $a$ , we obtain a whole family of results. There are no limitations in the selection of the value of the coefficient  $a$  as long as the value is real, although Jo et al. (1996) suggest a search in the region  $0 \leq a \leq 1$  for practical purposes. The optimal value of coefficient  $a$  must be sought to maximize the accuracy of the solution for all propagation directions. In other words, we seek to combine the two solutions to minimize the numerical anisotropy.

Adequate second-order, finite-difference approximations for partial derivatives for equations (1), (2), (7), and (8) in each coordinate system can be found in Kelly et al. (1976) and are unchanged in this approach. For completeness, we give the difference formulas required for the rotated scheme. The approximations used for the nonmixed partial derivatives in the  $45^\circ$  coordinate system are

$$\left( \frac{\partial^2 v}{\partial x'^2} \right)_{m,n} \approx \frac{v_{m+1,n+1} - 2v_{m,n} + v_{m-1,n-1}}{2\Delta^2} \quad (15)$$

and

$$\left(\frac{\partial^2 v}{\partial z'^2}\right)_{m,n} \approx \frac{v_{m-1,n+1} - 2v_{m,n} + v_{m+1,n-1}}{2\Delta^2}, \quad (16)$$

where  $\Delta$  is the grid spacing in  $x$  and  $z$  directions and  $m, n$  are discrete grid point coordinates. To better visualize the computations implied by equations (15) and (16) and similar equations to follow, we will present these as computational stars:

$$\left(\frac{\partial^2}{\partial x'^2}\right) \approx \frac{1}{2\Delta^2} \begin{bmatrix} 0 & 0 & 1 \\ 0 & -2 & 0 \\ 1 & 0 & 0 \end{bmatrix} \left(\frac{\partial^2}{\partial z'^2}\right) \approx \frac{1}{2\Delta^2} \begin{bmatrix} 1 & 0 & 0 \\ 0 & -2 & 0 \\ 0 & 0 & 1 \end{bmatrix}. \quad (17)$$

The mixed finite-difference term in the rotated frame of reference, using the star shown in Figure 1c, is given by

$$\left(\frac{\partial^2 v}{\partial x' \partial z'}\right)_{m,n} \approx \frac{v_{m-1,n} + v_{m+1,n} - v_{m,n+1} - v_{m,n-1}}{2\Delta^2} \quad (18)$$

or

$$\left(\frac{\partial^2}{\partial x' \partial z'}\right) \approx \frac{1}{2\Delta^2} \begin{bmatrix} 0 & -1 & 0 \\ 1 & 0 & 1 \\ 0 & -1 & 0 \end{bmatrix}. \quad (19)$$

### Consistent and lumped mass terms

The previous discussion targeted the differential parts of the equations. This led to a scheme to minimize the amount of numerical anisotropy. To minimize the overall numerical dispersion, we now concentrate on the algebraic terms  $\rho\omega^2 u$  and  $\rho\omega^2 v$  in equations (13) and (14). These terms are normally approximated by using the value of the density and the field variable  $u$  or  $v$  at each local node point. This is known as a consistent formulation. An alternative formulation, known in finite-element methods as a lumped formulation, is obtained by using an interpolation of the field values from the nearest node points, where the interpolation is weighted by the local mass (density) (Zienkiewicz and Taylor, 1989; Jo et al., 1996). If we combine the consistent and lumped mass methods by a weighted average, the required terms for homogeneous media (with constant  $\rho$ ) become

$$\rho\omega^2 v_{m,n} \approx \rho\omega^2 b v_{m,n} + \rho\omega^2 \frac{(1-b)}{4} \times (v_{m+1,n} + v_{m-1,n} + v_{m,n+1} + v_{m,n-1}), \quad (20)$$

where the coefficient  $b$ , as with the combined rotated schemes, is chosen to minimize the numerical errors. Here we have only used the values from the five-point star, and we have ignored the values from the corners of the nine-point star. This is because we have found through numerical testing that the optimal weighting for these points is always close to zero, a result consistent with that obtained by Jo et al. (1996) for the acoustic scheme.

The final differencing scheme for the 2-D, homogeneous, viscoelastic wave equation is obtained by combining the finite-difference approximations for equations (13) and (14) with equation (20). The complete scheme is given in Appendix A as equations (A-1) and (A-2).

We now have a total scheme that (i) minimizes numerical anisotropy (by an appropriate choice of the weighting factor  $a$ ) and (ii) minimizes overall numerical dispersion (by an appropriate choice of the weighting factor  $b$ ). All that remains is to determine the optimal values of the two weighting parameters,  $a$  and  $b$ . These parameters are determined by searching for values that provide a minimum of numerical anisotropy and numerical dispersion over the range of expected values of velocity. In the next section of this paper we describe the manner of optimally selecting parameters  $a$  and  $b$ . Note that  $a$  and  $b$  are not independent and must be determined simultaneously. Before proceeding to the optimization scheme, we will comment briefly on the scheme for the heterogeneous wave equation.

### Heterogeneous formulation

The approach used in the previous three sections for the homogeneous viscoelastic wave equation can also be applied to the equivalent wave equation for heterogeneous media, in which the elastic constants  $\lambda$  and  $\mu$  and the density  $\rho$  are free to vary from one node point to the next.

The partial differential equations for viscoelastic wave propagation in heterogeneous 2-D media are

$$\begin{aligned} \rho\omega^2 u + \frac{\partial}{\partial x} \left[ \lambda \left( \frac{\partial u}{\partial x} + \frac{\partial v}{\partial z} \right) + 2\mu \frac{\partial u}{\partial x} \right] \\ + \frac{\partial}{\partial z} \left[ \mu \left( \frac{\partial v}{\partial x} + \frac{\partial u}{\partial z} \right) \right] = 0 \end{aligned} \quad (21)$$

and

$$\begin{aligned} \rho\omega^2 v + \frac{\partial}{\partial z} \left[ \lambda \left( \frac{\partial u}{\partial x} + \frac{\partial v}{\partial z} \right) + 2\mu \frac{\partial v}{\partial z} \right] \\ + \frac{\partial}{\partial x} \left[ \mu \left( \frac{\partial v}{\partial x} + \frac{\partial u}{\partial z} \right) \right] = 0. \end{aligned} \quad (22)$$

In an analogous manner to the approach used for homogeneous media, we substitute  $u, v, x$ , and  $z$  with  $u', v', x'$ , and  $z'$  to obtain equations in a 45° rotated coordinate system and a new, mixed system of partial differential equations in heterogeneous media:

$$\begin{aligned} \rho\omega^2 u + a \left\{ \frac{\partial}{\partial x} \left[ \lambda \left( \frac{\partial u}{\partial x} + \frac{\partial v}{\partial z} \right) + 2\mu \frac{\partial u}{\partial x} \right] \right. \\ \left. + \frac{\partial}{\partial z} \left[ \mu \left( \frac{\partial v}{\partial x} + \frac{\partial u}{\partial z} \right) \right] \right\} + \frac{(1-a)}{2} \\ \times \left\{ \frac{\partial}{\partial x'} \left[ \lambda \left( \frac{\partial u}{\partial x'} + \frac{\partial v}{\partial x'} + \frac{\partial v}{\partial z'} - \frac{\partial u}{\partial z'} \right) + 2\mu \left( \frac{\partial u}{\partial x'} + \frac{\partial v}{\partial x'} \right) \right] \right. \\ \left. + \frac{\partial}{\partial z'} \left[ \mu \left( \frac{\partial v}{\partial x'} - \frac{\partial u}{\partial x'} + \frac{\partial u}{\partial z'} + \frac{\partial v}{\partial z'} \right) \right] \right. \\ \left. - \frac{\partial}{\partial z'} \left[ \lambda \left( \frac{\partial u}{\partial x'} + \frac{\partial v}{\partial x'} + \frac{\partial v}{\partial z'} - \frac{\partial u}{\partial z'} \right) + 2\mu \left( \frac{\partial v}{\partial z'} - \frac{\partial u}{\partial z'} \right) \right] \right. \\ \left. - \frac{\partial}{\partial x'} \left[ \mu \left( \frac{\partial v}{\partial x'} - \frac{\partial u}{\partial x'} + \frac{\partial u}{\partial z'} + \frac{\partial v}{\partial z'} \right) \right] \right\} = 0 \end{aligned} \quad (23)$$

and

$$\begin{aligned} \rho\omega^2 v + a \left\{ \frac{\partial}{\partial z} \left[ \lambda \left( \frac{\partial u}{\partial x} + \frac{\partial v}{\partial z} \right) + 2\mu \frac{\partial v}{\partial z} \right] + \frac{\partial}{\partial x} \left[ \mu \left( \frac{\partial v}{\partial x} + \frac{\partial u}{\partial z} \right) \right] \right\} + \frac{(1-a)}{2} \left\{ \frac{\partial}{\partial x'} \left[ \lambda \left( \frac{\partial u}{\partial x'} + \frac{\partial v}{\partial x'} + \frac{\partial v}{\partial z'} - \frac{\partial u}{\partial z'} \right) \right] \right. \\ \left. + 2\mu \left( \frac{\partial u}{\partial x'} + \frac{\partial v}{\partial x'} \right) \right\} + \frac{\partial}{\partial z'} \left[ \mu \left( \frac{\partial v}{\partial x'} - \frac{\partial u}{\partial x'} + \frac{\partial u}{\partial z'} + \frac{\partial v}{\partial z'} \right) \right] \\ + \frac{\partial}{\partial z'} \left[ \lambda \left( \frac{\partial u}{\partial x'} + \frac{\partial v}{\partial x'} + \frac{\partial v}{\partial z'} - \frac{\partial u}{\partial z'} \right) + 2\mu \left( \frac{\partial v}{\partial z'} - \frac{\partial u}{\partial z'} \right) \right] \\ \left. + \frac{\partial}{\partial x'} \left[ \mu \left( \frac{\partial v}{\partial x'} - \frac{\partial u}{\partial x'} + \frac{\partial u}{\partial z'} + \frac{\partial v}{\partial z'} \right) \right] \right\} = 0. \quad (24) \end{aligned}$$

As before,  $a$  is a weighting term used to control the relative importance of the two coordinate systems used in this mixed equation.

Equations (23) and (24) must then be finite differenced. Once again, we use the differencing stars given by (Kelly et al. (1976) to produce the required operators. As an illustration we present the four required difference operators for the rotated coordinate system as finite-difference stars, using the symbol  $v$  to represent either of the Lamé parameters,  $\lambda$  or  $\mu$ :

$$\frac{\partial}{\partial x'} \left( v \frac{\partial}{\partial x'} \right) \approx \frac{1}{2\Delta^2} \begin{array}{|c|c|c|} \hline 0 & 0 & v_+^+ \\ \hline 0 & -(v_+^+ + v_-^-) & 0 \\ \hline v_-^- & 0 & 0 \\ \hline \end{array}, \quad (25)$$

$$\frac{\partial}{\partial z'} \left( v \frac{\partial}{\partial z'} \right) \approx \frac{1}{2\Delta^2} \begin{array}{|c|c|c|} \hline v_-^+ & 0 & 0 \\ \hline 0 & -(v_-^+ + v_+^-) & 0 \\ \hline 0 & 0 & v_+^- \\ \hline \end{array}, \quad (26)$$

$$\frac{\partial}{\partial x'} \left( v \frac{\partial}{\partial z'} \right) \approx \frac{1}{2\Delta^2} \begin{array}{|c|c|c|} \hline 0 & -v_+^+ & 0 \\ \hline v_-^- & 0 & v_+^+ \\ \hline 0 & -v_-^- & 0 \\ \hline \end{array}, \quad (27)$$

and

$$\frac{\partial}{\partial z'} \left( v \frac{\partial}{\partial x'} \right) \approx \frac{1}{2\Delta^2} \begin{array}{|c|c|c|} \hline 0 & -v_-^+ & 0 \\ \hline v_+^+ & 0 & v_-^- \\ \hline 0 & -v_-^+ & 0 \\ \hline \end{array}, \quad (28)$$

where the parameters ( $v$ ) at intermediate (i.e., staggered) grid points are represented by

$$v_{\pm}^{\pm} = v_{m \pm \frac{1}{2}, n \pm \frac{1}{2}} = \frac{1}{2}(v_{m,n} + v_{m \pm 1, n \pm 1}). \quad (29)$$

These four stars specify all required finite-difference operators for the rotated coordinate system; the remaining operators for the original coordinate system are unchanged from Pratt

(1990). The approach used for the lumped and consistent mass terms is introduced in exactly the same manner as for the homogeneous case [see equation (20)], except that the density value must also be averaged from the neighboring node points along with the field variables.

The final system for modeling the 2-D, heterogeneous, viscoelastic wave equation is thus fully specified, apart from the weighting parameters,  $a$ , the relative amount of the original, unrotated second-order scheme, and  $b$ , the relative amount of the consistent mass term with respect to the lumped mass term. In the absence of a scheme for evaluating the optimal parameters for a heterogeneous media, the weighting parameters are obtained by returning to the homogeneous formulation and choosing values that provide minimum numerical errors.

## NUMERICAL ERRORS AND OPTIMIZATION

### Determination of optimal coefficients

To fully specify our new differencing scheme, we now must determine values for the weighting coefficient  $a$  in equations (13), (14), (23), and (24) and for  $b$  in equation (20). To minimize the errors, we must be able to predict the numerical errors for a particular choice of  $a$  and  $b$ . The numerical errors are predicted in a standard fashion by assuming a plane-wave solution for the homogeneous scheme and solving the resultant system for the numerical compressional and shear-wave velocities. The required analysis is detailed in Appendix A. The final equations depend on  $a$ ,  $b$ ,  $\sigma$ ,  $K$ , and  $\theta$ , where  $\sigma$  is Poisson's ratio of the elastic medium,  $K$  is the wavenumber in grid point units (i.e.,  $K = 1/G$ , where  $G$  is the number of grid points per wavelength), and  $\theta$  is the propagation angle (both positive and negative) relative to the  $x$  or  $z$  directions on the original grid.

The method applied for determining the coefficients closely follows the method suggested by Jo et al. (1996): We search for a set of values for  $a$  and  $b$  that minimize a given misfit function, using a representative value of Poisson's ratio. The misfit function measures the aggregate misfit of the error in the numerical group velocities over a range of possible values of  $K$  (governed by the range in true velocities in the medium) and over a range of propagation angles. Formally, we minimize

$$F(a, b, \sigma) = \int_0^{0.5} \int_0^{\pi/4} \max\{F_p(a, b, \sigma, K, \theta), F_s(a, b, \sigma, K, \theta)\} dK d\theta, \quad (30)$$

where

$$F_p(a, b, \sigma, K, \theta) = \left| 1 - \frac{\hat{v}_{pg}(a, b, \sigma, RK, \theta)}{v_{pg}} \right|^2 \quad (31)$$

and

$$F_s(a, b, \sigma, K, \theta) = \left| 1 - \frac{\hat{v}_{sg}(a, b, \sigma, K, \theta)}{v_{sg}} \right|^2. \quad (32)$$

In equations (31) and (32),  $K$  is the number of grid points per shear wavelength,  $R = \sqrt{(0.5 - \sigma)/(1 - \sigma)}$  is the  $v_s/v_p$  ratio in the medium,  $v_{pg}$  and  $v_{sg}$  are the (true) compressional and shear wave group velocities, and  $\hat{v}_{pg}$  and  $\hat{v}_{sg}$  are the numerical

group velocities, for which explicit expressions in terms of the variables ( $a, b, \sigma, K, \theta$ ) are given in Appendix A.

For a given value of  $\sigma$ , we have only two unknown parameters. It is therefore possible to evaluate the function  $F(a, b, \sigma)$  for a reasonable range of values of  $a$  and  $b$  and to plot this function as a surface. The optimal values can then be estimated and the procedure can be repeated on a tighter interval near the optimal point. This was the procedure used to determine  $a$  and  $b$  for the examples that follow. The coefficients  $a$  and  $b$  in general depend on Poisson's ratio used in the model. If this is expected to vary widely, one could include an integral over possible Poisson ratios in the misfit function. In Figure 2 the optimum values of the parameters as a function of Poisson's ratio are shown. While the optimal value of the ratio between consistent and lumped mass matrix methods,  $b$ , is relatively stable, for large Poisson ratios (i.e., for near fluids) the weighting of the unrotated scheme (parameter  $a$ ) approaches zero. This is consistent with the expectation that the ordinary second-order scheme cannot handle fluids (Stephen, 1983; Virieux, 1986; Kerner, 1990). We shall return to the fluid case in a later section, when we show that the scheme predicts no numerical dispersion for shear waves in fluids, a necessary condition for being able to model liquid-solid interfaces.

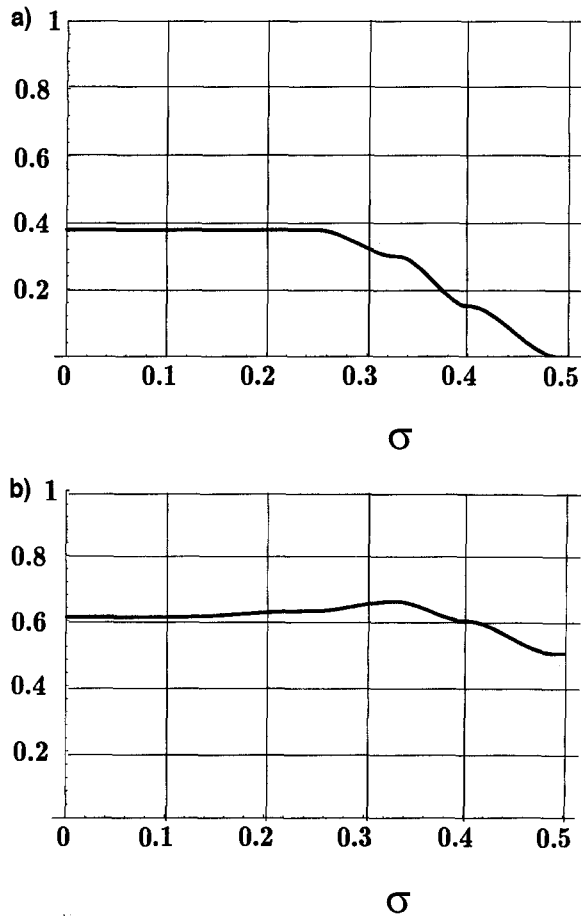


FIG. 2. Optimal values of coefficients  $a$  (the fraction of the ordinary second order scheme) and  $b$  (the fraction of the consistent mass matrix), plotted as a function of Poisson's ratio,  $\sigma$ . The optimal value of coefficient  $a$  decreases for high values of  $\sigma$  and becomes 0 for the fluid case, in which case only the rotated scheme is used. The optimal value of coefficient  $b$  is relatively insensitive to the value of  $\sigma$ .

### Numerical dispersion

In this section we present some representative dispersion analyses for the combined scheme discussed in this paper. The analysis is generated using the choice of weighting parameters  $a$  and  $b$  depicted in Figure 2 and the dispersion analysis given in Appendix A. Figures 3 and 4 depict the normalized numerical phase and group velocities (for both compressional and shear waves), using the standard second-order scheme (left column) and the new optimally combined scheme (right column). A value of 1.0 for the normalized velocity represents an error-free numerical result; in all figures, this is achieved when  $K = 1/G$  (the wavenumber in grid point units) is zero.

From Figure 3 it is evident that the original second-order scheme yielded good, isotropic, undispersed results for the compressional-wave phase velocities but very poor phase and group results for shear waves. The original scheme also yielded a nearly isotropic result for compressional-wave phase and group velocities but contained errors of more than 8% at four grid points per wavelength (0.25 on the horizontal axes) for the compressional-wave group velocity. The new combined scheme introduces a small amount of numerical anisotropy into the compressional-wave results and slightly decreases the group velocity dispersion for  $P$ -waves, yielding a much improved  $S$ -wave performance. Figure 4, in which Poisson's ratio has been increased to 0.4, is similar to Figure 3 (except the shear-wave dispersion is much more severe for the standard second-order scheme). Again, the combined scheme introduces a small amount of numerical anisotropy into the compressional-wave velocities but decreases the overall velocity dispersion for compressional waves and yields a dramatically improved shear-wave performance. In contrast to the standard second-order scheme, the new scheme is thus able to cope well with a range of Poisson ratios.

### Modeling in fluids

Standard second-order schemes generate infinite dispersion for shear waves when used to simulate propagation in liquid layers (Bamberger et al., 1980; Stephen, 1983). This problem has effectively been solved for time-domain modeling by Virieux (1986) and others (Kerner, 1990), in which the coupled, first-order, elastodynamic system, rather than the second-order wave equation, is simulated on a staggered numerical grid. Let us examine the performance of the new scheme in fluid layers. In Figure 2 we showed that the optimal value of parameter  $a$  (the fraction of the standard scheme) approaches zero as Poisson's ratio,  $\sigma$ , approaches 0.5. This is a direct consequence of the behavior of the standard scheme at large Poisson ratios. Therefore, in pure fluids, we will have to use the rotated scheme only ( $a = 0$ ). We now show analytically that the rotated scheme predicts the true shear-wave behavior in fluids ( $v_s = 0.0$ ).

We follow closely the dispersion analysis given in Appendix A. Equation (A-5) predicts the normalized, numerical shear-wave group velocity. This equation cannot be used where the true shear velocity,  $v_s$ , is zero, as  $v_s$  appears on the denominator of equation (A-5). However, a similar expression for the non-normalized, numerical shear velocity can be obtained:

$$\hat{v}_{sp} = \frac{v_p}{2\pi K} \sqrt{\frac{\gamma_1 - \sqrt{\gamma_1^2 - 4\gamma_2\alpha_3}}{2\alpha_3}}, \quad (33)$$

where the coefficients are the same as those defined for equation (A-5). Inserting  $a = 0$  into the coefficients we find that, for  $R = 0$  (because  $v_s = 0$ ),

$$\begin{aligned}\alpha_1 &= [-1 + \cos \bar{\kappa}_x - \cos \bar{\kappa}_z + \cos \bar{\kappa}_x \cos \bar{\kappa}_z], \\ \alpha_2 &= [-1 - \cos \bar{\kappa}_x + \cos \bar{\kappa}_z + \cos \bar{\kappa}_x \cos \bar{\kappa}_z], \\ \alpha_3 &= b + \frac{(1-b)}{2} (\cos \bar{\kappa}_x + \cos \bar{\kappa}_z), \quad \gamma_1 = \alpha_3(\alpha_1 + \alpha_2),\end{aligned}$$

and

$$\gamma_2 = \alpha_2 \alpha_1 - \sin^2 \bar{\kappa}_x \sin^2 \bar{\kappa}_z,$$

where, as in Appendix A,  $\bar{\kappa}_x$  and  $\bar{\kappa}_z$  are the wave-vector components in grid point units. Inserting these simplified coefficients back into equation (33) yields

$$\hat{v}_{Sp} = \frac{v_p}{2\pi K} \sqrt{\frac{(\alpha_1 + \alpha_2) - \sqrt{(\alpha_1 + \alpha_2)^2 - 4\gamma_2}}{2}}. \quad (34)$$

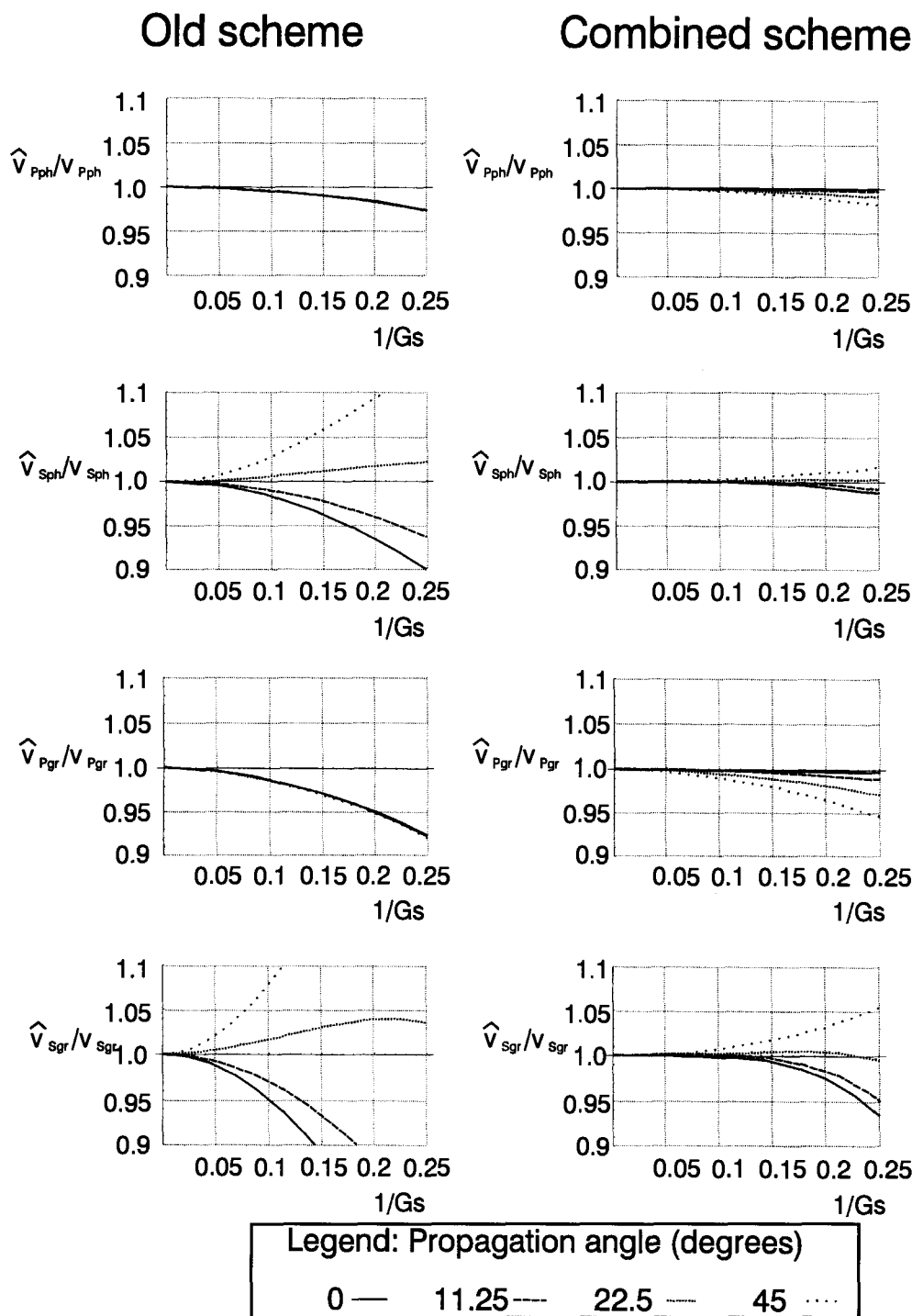


FIG. 3. Numerical dispersion of the new scheme for a Poisson ratio  $\sigma = 0.33$ , depicting normalized numerical velocity curves for compressional and shear phase velocities (top two rows) and group velocities (bottom two rows). Results are presented for the standard second-order scheme (left column) and the new combined scheme (right column). The dispersion curves are plotted against the shear wavenumber in grid point units. See text for the meaning of the symbols used on the vertical axes.



Further algebraic manipulation reveals that  $\gamma_2 = 0$ , from which it is then obvious that  $\hat{v}_{sp} = 0$  (for all values of  $K$ ).

Thus, the new, rotated scheme, used on its own, gives the exact shear-wave phase velocity ( $v_{sp} = 0$ ) in a fluid. An exact, constant, numerical-phase velocity for all wavenumbers implies the numerical group velocity ( $\hat{v}_g = \partial\omega/\partial\kappa$ ) is also exact. Interestingly, the rotated scheme generates a differencing scheme that has certain similarities with the staggered-grid differencing

schemes used by Virieux (1986) and Kerner (1990) to solve the fluid layer problem.

The compressional-wave group and phase dispersion in a fluid for the new scheme are depicted in Figure 5. These results show that the numerical dispersion for compressional wave in fluids can be significant with the new scheme. However, errors of less than 5% can be achieved with 7–8 grid points per wavelength.

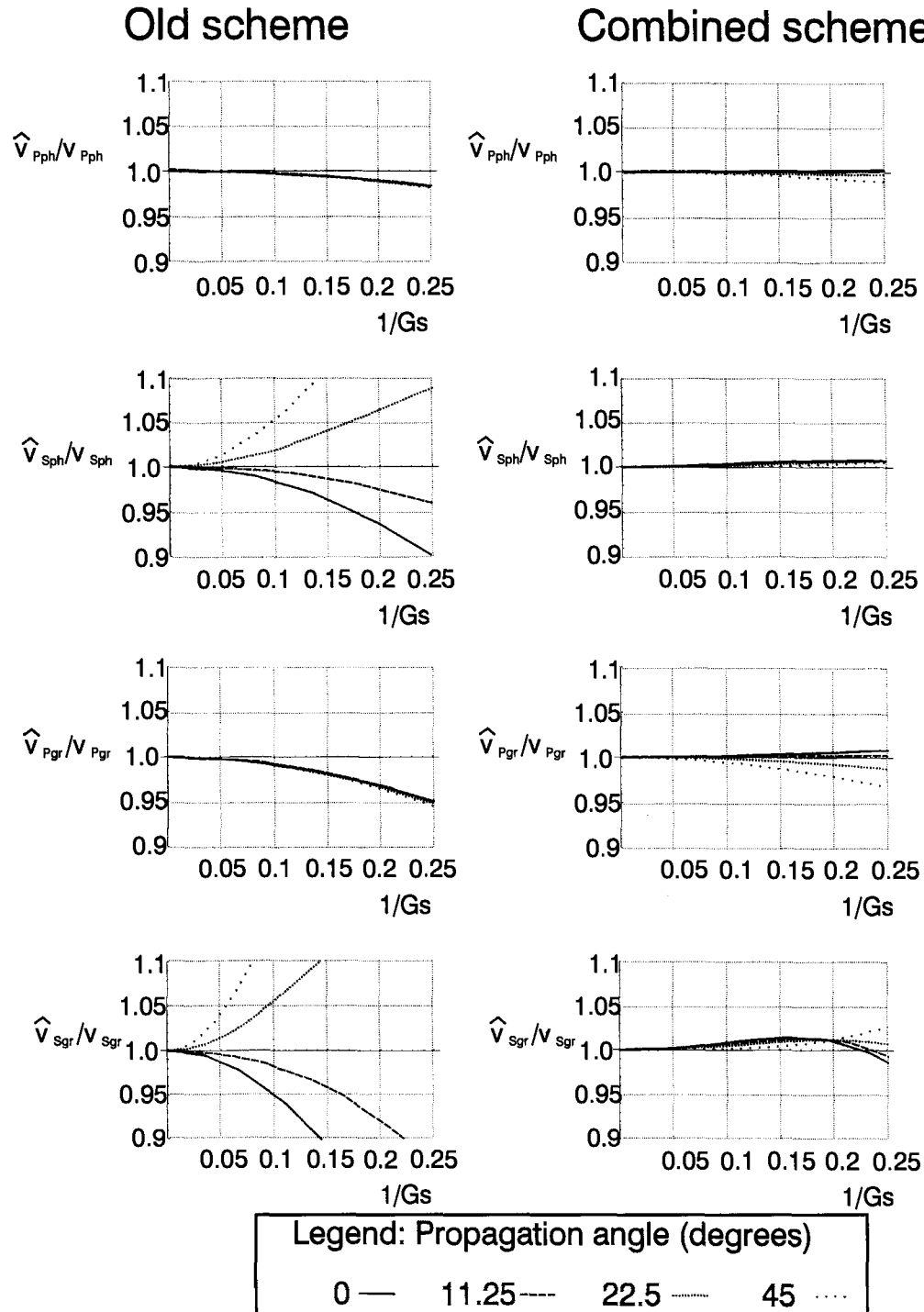


FIG. 4. Numerical dispersion for a Poisson ratio  $\sigma = 0.4$ , depicting normalized numerical velocity curves for compressional and shear phase velocities (top two rows) and group velocities (bottom two rows). Results are presented for both the standard second-order scheme (left column) and the new combined scheme (right column). The dispersion curves are plotted against the shear wavenumber in grid point units. See text for the meaning of the symbols used on the vertical axes.

## Discussion

It is evident that our new, combined scheme performs better than the standard second-order scheme for a wide range of Poisson ratios. (Naturally, the optimized scheme is no worse than any single scheme.) When compared with Marfurt's (1984a) optimal frequency-domain (finite-element) scheme, our new combined scheme provides better accuracy in cases where  $\sigma$  is greater than approximately 0.3. For values of  $\sigma$  less than 0.3, the combined scheme gives results comparable to Marfurt's optimal finite-element scheme, with a slightly higher numerical anisotropy.

In seeking the shape of the optimal differencing star, we tried to minimize the spatial extent of the star to preserve the numerical bandwidth of the finite-difference matrix. We achieved a considerable increase in accuracy with a nine-point differencing star for the combined scheme. The question therefore arises as to whether a larger differencing star—possibly using higher order differencing formulas—might lead to further computational savings. The inclusion of any additional points will increase the numerical bandwidth of the matrix and increase the computational overheads. If this increase were balanced by a corresponding decrease in the number of grid points required per wavelength, then this would be acceptable. However, in Appendix B we show that the optimal finite-difference operator must, in fact, be limited to the nine-point star of Figure 1(c).

[This conclusion is coupled to the use of the (optimal) nested dissection method (George and Liu, 1981) to reorder and solve the matrix equations. If a simpler, but more expensive, band-ordered solver is used, the conclusions are different. However, for large problems, one could not consider frequency-domain finite differences without the use of a nested dissection solver or a similar optimal solver.]

By using a linear combination of two schemes, we in fact distorted the isotropic nature of the original scheme for modeling compressional waves and thereby gained a higher accuracy for shear waves. For most Poisson ratios, the rotated scheme models shear waves better than compressional waves, while the original scheme gives the opposite results. The fraction of each scheme (the  $a$  coefficient) appears to control the relative accuracy for compressional and shear waves and thus acts as a tradeoff factor. The other parameter (the  $b$  coefficient) controls the overall dispersion for a given linear combination of both the standard and rotated schemes. Clearly, there is room for customizing the scheme in certain situations. By choosing critical data phases and choosing alternative values of parameters  $a$  and  $b$ , it would be possible to obtain a scheme that requires even fewer grid points per wavelength and obtain the same, or better, accuracy for any given, specific phase.

If the model contains a range of Poisson ratios, then there may be inaccuracies in regions in which the Poisson ratio differs largely from that used in the selection of parameters  $a$  and  $b$ .

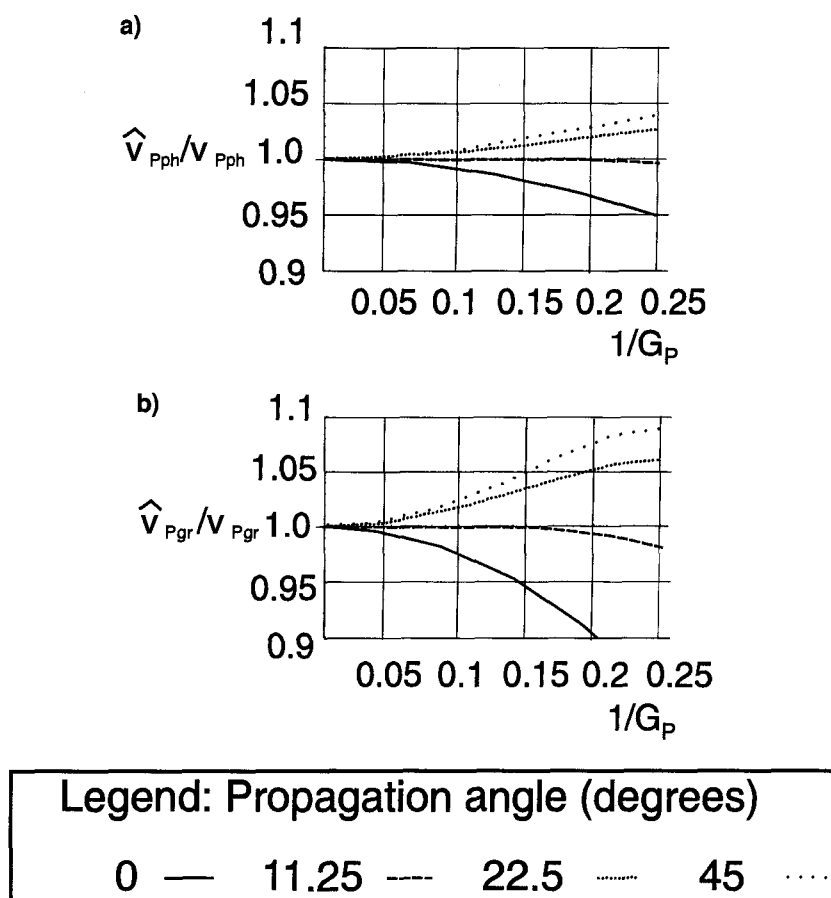


FIG. 5. Compressional wave dispersion in fluids for the new, rotated scheme. In the fluid case we use only the rotated scheme, with no component of the original, unrotated scheme ( $a = 0$ ). (a) Normalized compressional phase velocities. (b) Normalized compressional group velocities.

Fortunately, from Figure 2, the values of the parameters are relatively stable over a range of Poisson ratios. Only at large values of Poisson's ratio is there an indication of a need to adjust these parameters. In heterogeneous models it may then be necessary to adjust these locally. A local variation of coefficients for variable Poisson ratios is also suggested for the finite-element method by Marfurt (1984a). The effect of using variable coefficients within the same model is unclear, although initial numerical tests look promising.

One effect of the use of a rotated differencing scheme is that any interface, dipping or flat, is treated as a staircase in the model because at least one scheme is not aligned with the interface. This leads to regular, low-intensity grid diffractions on the interfaces. Such grid diffractions are common for dipping layers with standard schemes, and we do not consider the presence of these diffractions for flat interfaces to be a serious drawback. Muir et al. (1992) points out a simple scheme based on transversely effective media for minimizing these effects; Zeng and West (1996) also give a scheme for minimizing these effects based on a simple smoothing of the model.

### ELASTIC MODELING EXAMPLE

Verification of our modeling scheme has been carried out in several standard models. Rather than showing these obvious results here, we now demonstrate the new scheme using the class of complex medium for which the scheme was designed: studying crosshole seismic data from a layered and faulted sedimentary sequence in which a high level of attenuation exists. The data come from the Imperial College test site at

Whitcheater in northern England. The site consists of cyclically layered, interbedded mudstones, sandstones, and carbonates [detailed in Pratt and Sams (1996) and Neep et al. (1996)].

The crosshole data were acquired between two boreholes at the test site penetrating the top 220 m of the sequence and separated by 75 m (the boreholes are at the left and right edges of Figure 6). The acquisition was carried out using a clamped piezoelectric transmitter and hydrophone receivers. The transmitter was driven with a pseudo-random binary signal at a central frequency of 400 Hz. The source was positioned in the first borehole (the left side of the figures), and recordings were made from each source position at receivers positioned every 2 m between 17 and 217 m in the second borehole (on the right side of the figures).

The geology of the target is illustrated schematically by the overlay on Figure 6. The largest velocity contrasts in the sequence are at depths of 145 and 170 m, where two high-velocity carbonate layers beds are found with thicknesses of 5 and 10 m, respectively. The only structural feature in the section is a small, steep, right-dipping normal fault crossing borehole 1 at 120 m with a vertical displacement of approximately 10 m.

The grayscale image in Figure 6 is a representation of the *P*-wave velocity variations we use in our forward model of wave propagation at the site. This model is the result of an earlier study in full wavefield inversion (Pratt et al., 1995; Pratt and Shipp, 1998), using an acoustic inversion routine, after the method described by Song et al. (1994). The high-velocity carbonates are easily identified; it is also possible to identify the location of the normal fault from the truncations of these carbonates toward the left of the image.

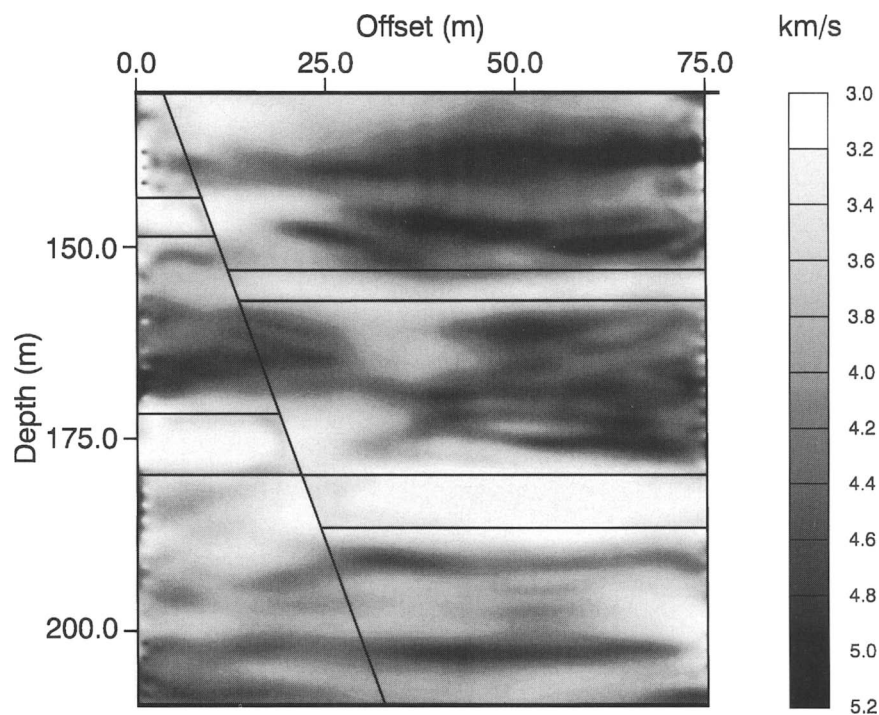


FIG. 6. *P*-wave velocity model for the Imperial College crosshole experiment. The model was obtained using acoustic full-wave inversion (Pratt et al., 1995). The overlay shows the known stratigraphic and structural features obtained from borehole information. The prominent high-velocity zones, truncated by the fault, correspond to carbonate sediments. Real data from the crosshole experiment and modeled data for this velocity structure are shown in Figures 7 and 8.

Figure 7a depicts the seismic data from a representative raw common source gather, and Figure 7b depicts the result of acoustic forward modeling in the velocity model shown in Figure 6. The acoustic modeling reproduces the arrival times nearly exactly and predicts much of the character of the waveform within the first 5 ms of the first arrival. There is, however, little correspondence between the predicted and observed wavefields at late time. The modeling fails to generate the large-amplitude incoherent events observed 10–20 ms following the first arrivals.

To study the remaining discrepancies between observed and predicted data, we built a fully viscoelastic model from the  $P$ -wave velocities in Figure 6 using the following assumptions: First, the  $S$ -wave velocities are assumed to be everywhere 50% of the  $P$ -wave velocities. Next, since the rocks at the site are known to be highly attenuating (Neep et al., 1996), we incorporated inelastic attenuation by assuming that the  $P$  and  $S$  quality factors were each constant over all frequencies and homogeneous. We selected a quality factor of  $Q_p = 50$  for the  $P$ -waves and  $Q_s = 20$  for the  $S$ -waves. Appropriate complex-valued Lamé parameters for this elastic model were separately computed at each frequency, after Müller (1983). Finally, we

modeled the source by using a horizontal point force introduced into the numerical mesh at the source location. A total of 240 separate frequencies were modeled, and time domain records were produced by Fourier summation of the results. The largest frequency used in the modeling was 1000 Hz; the lowest  $S$ -wave velocity was 1000 km/s. We used  $G_s = 0.25$  (i.e., four grid points per shear wavelength), resulting in a grid interval of 0.25 m and a model with  $300 \times 320 = 96\,000$  grid points. For Poisson's ratio we used  $\sigma = 0.33$ . The optimal weighting parameters for the rotated scheme and for the lumped mass scheme are  $a = 0.33$  and  $b = 0.66$ .

The site exhibits significant elastic anisotropy [as reported by Pratt, (1996)], with  $P$ -wave velocities 20% faster in the horizontal direction than in the vertical direction. Although the modeling scheme has not been extended to the anisotropic case (an extension to simple transverse isotropy would be feasible but has not yet been carried out), we effected a simulation of the anisotropy by compressing the horizontal distances in the model by 20%, thus creating the kinematic equivalent of an elliptically anisotropic media with a vertical symmetry axis. This is consistent with the manner in which the anisotropy was simulated by Pratt et al. (1995) and predicts the correct traveltimes.

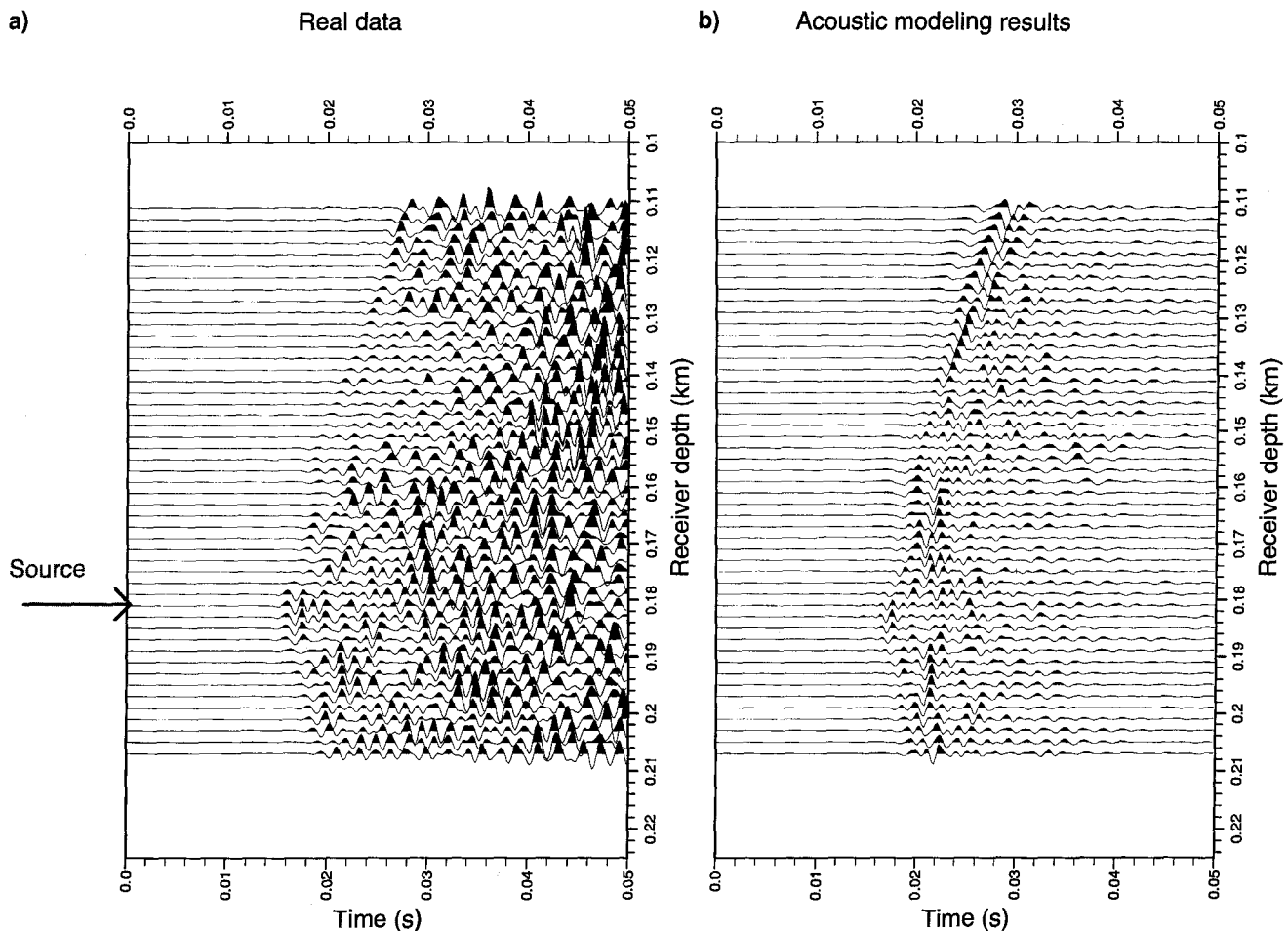


FIG. 7. (a) A representative common source gather from the crosshole data collected at the Imperial College test site. The S/N ratio is high, and the first-arrival waveforms are clear and coherent. At late times, incoherent large-amplitude arrivals dominate. (b) Predicted common source data using acoustic forward modeling in the velocity structure shown in Figure 6. The first-arrival traveltimes and waveforms match well with the observed data, but the large-amplitude late arrivals are not predicted with the acoustic method.

The results of viscoelastic modeling using our new scheme are shown on Figures 8a and b. The modeling synthesizes the horizontal and vertical components of displacement. A direct comparison of these data with the borehole pressure measured by the hydrophones in the field cannot easily be made; the relationship is complicated and highly dependent on a number of poorly controlled variables (Peng et al., 1993). (The dilatation, which measures the  $P$ -wave energy in the formation, is a poor predictor of borehole pressure because it does not take into account, for example, conversion of  $S$ -waves at the borehole wall.) However, a qualitative comparison can be made with the modeled displacements. The horizontal component shows first-arrival times and waveforms similar to the acoustic modeling results and some high-amplitude arrivals at late times. The vertical component shows high-amplitude, incoherent arrivals similar to those observed on the real data. There is no exact match between these late arrivals and the observed data. Nevertheless, even with the simple assumptions we have made in building the viscoelastic model from the  $P$ -wave velocity model, we managed to create synthetic viscoelastic data that look more like the data collected at the site than the synthetic acoustic-wave data. The late arrivals thus appear to be related to the mode conversion of  $P$ -wave energy into  $S$ -wave energy

within the heterogeneous model. One may speculate whether a better match in the times of the late arrivals could be achieved by adjusting the Poisson ratios in the model or even whether a formal viscoelastic inversion of the data from this experiment could be attempted.

### CONCLUSION

In this paper we have shown that it is possible to dramatically improve on standard second-order, finite-difference schemes for viscoelasticity without increasing computational costs. It would appear that former limitations on second-order schemes were because of the shape of the differencing operators. By reshaping these operators, one can accurately use models with high values of Poisson's ratio in a manner not previously possible with frequency-domain schemes. This has been achieved by extending the grid rotation technique proposed by Cole (1994) and Jo et al. (1996) to the viscoelastic case. For the 2-D viscoelastic case, we have shown there does not appear to be any possibility of achieving further improvements by searching for higher order spatial differencing schemes because of the associated computational overheads.

The rotated operator technique appears to be quite generally useful and worthy of testing in other applications of the

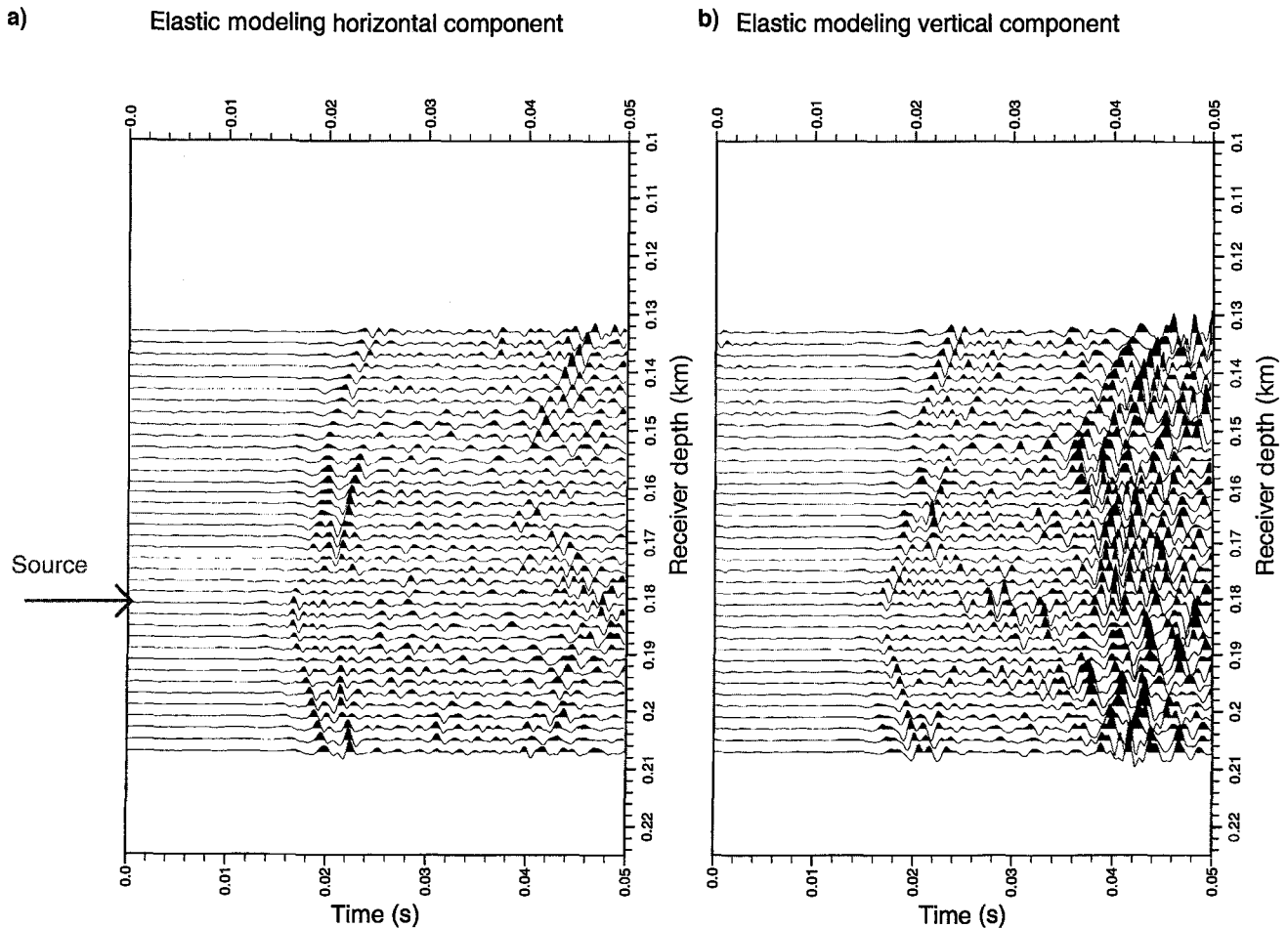


FIG. 8. Predicted common source data using the new viscoelastic modeling results. (a) Horizontal displacement component. (b) Vertical displacement component. The horizontal component shows first-arrival times and waveforms that are similar to the acoustic modeling results and some high-amplitude arrivals at late times. The vertical component shows high-amplitude arrivals similar to those observed on the real data.

finite-difference method. A substantial increase in accuracy is achieved with little or no increase in computational costs. We would expect significant improvements in three dimensions because of the possibility of combining rotations in each Cartesian plane with the original scheme.

We have shown analytically the improvements in accuracy for homogeneous media, and we have formally proven that the scheme predicts the correct shear-wave behavior in fluid layers. Using our numerical scheme, we were able to successfully model crosshole field data from a highly heterogeneous sedimentary environment known to be anisotropic and strongly attenuating. To do this, we made several simplifying assumptions (a constant Poisson's ratio; a homogeneous, constant  $Q$  attenuation; a homogeneous, elliptical anisotropy; and simple, point force source mechanisms). Nevertheless, we were able to generate a synthetic data set qualitatively consistent with the field data.

### ACKNOWLEDGMENTS

We thank the members of the Imperial College Exploration Seismology Research Consortium for providing the data used in this paper and the Overseas Research Scheme at Imperial College for financial support during the research. We also thank Gary Margrave and one anonymous reviewer for their helpful suggestions.

### REFERENCES

- Alterman, Z., and Karal, F. C., Jr. 1968, Propagation of elastic waves in layered media by finite difference methods: *Bull., Seis. Soc. Am.*, **58**, no. 1, 367–398.
- Bamberger, A., Chavent, G., and Lailly, P., 1980, Etude de schemas numeriques pour les equations de l'elastodynamique lineaire: INRIA (Institut National de Recherche en Informatique et en Automatique), **032-79**.
- Bouchon, M., Campillo, M., and Gaffet, S., 1989, A boundary integral equation-discrete wavenumber representation method to study wave propagation in multilayered media having irregular interfaces: *Geophysics*, **54**, 1134–1140.
- Campillo, M., and Bouchon, M., 1985, Synthetic SH-seismograms in a laterally varying medium by the discrete wavenumber method: *Geophys. J. Roy. Astr. Soc.*, **83**, 307–317.
- Carcione, J. M., 1995, Constitutive model and wave equations for linear, viscoelastic, anisotropic media: *Geophysics*, **60**, 537–548.
- Carcione, J. M., Kosloff, D., Behle, A., and Seriani, G., 1992, A spectral scheme for wave propagation simulation in 3-D elastic-anisotropic media: *Geophysics*, **57**, 1593–1607.
- Carcione, J. M., Kosloff, D., and Kosloff, R., 1988, Viscoacoustic wave propagation simulation in the earth: *Geophysics*, **53**, 769–777.
- Cole, J. B., 1994, A nearly exact second-order finite-difference time-domain wave propagation algorithm on a coarse grid: *Computers in Phys.*, **8**, 730–734.
- Dablain, M. A., 1986, The application of high-order differencing to the scalar wave equation: *Geophysics*, **51**, 54–66.
- Dai, N., Vafidis, A., and Kanasewich, E. R., 1995, Wave propagation in heterogeneous, porous media: A velocity-stress, finite-difference method: *Geophysics*, **60**, 327–340.
- Drake, L. A., 1972, Love and Rayleigh waves in non-horizontally layered media: *Bull., Seis. Soc. Am.*, **62**, 1241–1258.
- Dravinski, M., 1973, Scattering of plane harmonic SH-waves by dipping layers of arbitrary shapes: *Bull., Seis. Soc. Am.*, **63**, 1303–1319.
- Emmerich, H., and Korn, M., 1987, Incorporation of attenuation into time-domain computations of seismic wave fields: *Geophysics*, **52**, 1252–1264.
- Gazdag, J., 1981, Modeling of the acoustic wave equation with transform methods: *Geophysics*, **46**, 845–859.
- George, A., and Liu, J. W., 1981, Computer solution of large sparse positive definite systems: Prentice-Hall, Inc.
- Holdberg, O., 1987, Computational aspects of the choice of operator and sampling interval for numerical differentiation in large-scale simulation of wave phenomena: *Geophys. Prosp.*, **35**, 629–655.
- Jo, C. H., Shin, C. S., and Suh, J. H., 1996, An optimal 9-point, finite-difference, frequency-space, 2-D scalar wave extrapolator: *Geophysics*, **61**, 529–537.
- Kelly, K. R., Ward, R. W., Treitel, S., and Alford, R. M., 1976, Synthetic seismograms—a finite-difference approach: *Geophysics*, **41**, 2–27.
- Kerner, C., 1990, Modelling of soft sediments and liquid-solid interfaces: Modified wavenumber summation method and application: *Geophys. Prosp.*, **38**, 111–137.
- Kjartansson, E., 1979, Constant  $Q$ -wave propagation and attenuation: *J. Geophys. Res.*, **84**, 4737–4748.
- Marfurt, K. J., 1984a, Accuracy of finite-difference and finite-element modeling of the scalar and elastic wave-equations: *Geophysics*, **49**, 533–549.
- 1984b, Seismic modeling: A frequency-domain finite-element approach: Presented at the 54th Ann. Internat. Mtg., Soc. Expl. Geophys., Expanded Abstracts, 633–639.
- Mora, P., 1989, Modeling anisotropic seismic waves in 3-D: Presented at the 59th Ann. Internat. Mtg., Soc. Expl. Geophys., Expanded Abstracts, 1039–1043.
- Muir, F., Dellinger, J., Etgen, J., and Nichols, D., 1992, Modeling elastic fields across irregular boundaries (short note): *Geophysics*, **57**, 1189–1193.
- Müller, G., 1983, Rheological properties and velocity dispersion of a medium with power-law dependence of  $Q$  on frequency: *Geophysics*, **54**, 20–29.
- Neep, J. P., Sams, M. S., Worthington, M. H., and O'Hara-Dhand, K. A., 1996, Measurement of seismic attenuation from high-resolution crosshole data: *Geophysics*, **61**, 1175–1188.
- Peng, C., Cheng, C. H., and Toksoz, M. N., 1993, Borehole effects on downhole seismic measurements: *Geophys. Prosp.*, **41**, 883–912.
- Pratt, R. G., 1989, An improved seismic tomogram using the elastic wave equation: Presented at the 51st Ann. Mtg., Eur. Assn. Expl. Geophys., Technical Programme and Abstracts of Papers, 173–174.
- 1990, Frequency-domain elastic wave modeling by finite differences: A tool for crosshole seismic imaging: *Geophysics*, **55**, 626–632.
- Pratt, R. G., and Gouly, N. R., 1991, Combining wave-equation imaging with traveltimes tomography to form high-resolution images from crosshole data: *Geophysics*, **56**, 208–224.
- Pratt, R. G., and Sams, M. S., 1996, Reconciliation of crosshole seismic velocities with well information in a layered sedimentary environment: *Geophysics*, **61**, 549–560.
- Pratt, R. G., and Shipp, R. M., 1988, Seismic waveform inversion in the frequency domain—II: Fault delineation in sediments using crosshole data: *Geophysics*, in press.
- Pratt, R. G., Shipp, R. M., Song, Z. M., and Williamson, P. R., 1995, Fault delineation by wavefield inversion of cross-borehole seismic data: Presented at the 57th Ann. Mtg., Eur. Assoc. Expl. Geophys., Extended Abstracts, 1.
- Press, W. H., Teukolsky, S. A., Vetterling, W. T., and Flannery, B. P., 1992, Numerical recipes in FORTRAN: The art of scientific computing, 2nd Ed.: Cambridge Univ. Press.
- Robertsson, J. A., Blanch, J. O., and Symes, W. W., 1994, Viscoelastic finite difference modeling: *Geophysics*, **59**, 1444–1456.
- Schuster, G. T., 1984, A hybrid Bie & Born series modeling scheme: Generalized Born series: *J. Acoust. Soc. Am.*, **77**, 865–879.
- Smith, W. D., 1974, The application of finite element analysis to body wave propagation problem: *Geophys. J. Roy. Astr. Soc.*, **42**, 747–768.
- Song, Z. M., 1994, Frequency domain wave equation crosshole modelling and inversion: Ph.D. thesis, Imperial College of Science and Technology.
- Song, Z. M., Williamson, P. R., and Pratt, R. G., 1995, Frequency-domain acoustic-wave modeling and inversion of crosshole data: Part II—Inversion method, synthetic experiments and real data results: *Geophysics*, **60**, 796–809.
- Štekl, I., 1997, Frequency domain seismic forward modelling: A tool for waveform inversions: Ph.D. thesis, Imperial College London.
- Stephen, R. A., 1983, A comparison of finite difference and reflectivity seismograms: *Geophys. J. Roy. Astr. Soc.*, **72**, 39–57.
- Virieux, J., 1986,  $P$ - $SV$  wave propagation in heterogeneous media: Velocity-stress finite-difference method: *Geophysics*, **51**, 889–901.
- Zeng, X., and West, G. F., 1996, Reducing spurious diffractions in elastic wavefield calculations: *Geophysics*, **61**, 1436–1439.
- Zienkiewicz, O. C., and Taylor, R. L., 1989, The finite element method, 4th ed.: McGraw-Hill Book Co. (Div. of McGraw-Hill, Inc.).

## APPENDIX A

### DISPERSION ANALYSIS

If we take the second-order, finite-difference equations generated from equations (13) and (14) and use the combined consistent and lumped mass formulations for the density-weighted term in the viscoelastic wave equation (20), we obtain the following scheme for homogeneous media:

$$\begin{aligned} & \rho\omega^2 \left[ bu + \frac{(1-b)}{4}(u^+ + u^- + u_+ + u_-) \right] \\ & + a \left[ (\lambda + 2\mu) \frac{u^+ - 2u + u^-}{\Delta^2} + \mu \frac{u_+ - 2u + u_-}{\Delta^2} \right. \\ & + (\lambda + \mu) \frac{v_+^+ - v_+^- + v_-^+ - v_-^-}{4\Delta^2} \left. \right] + (1-a) \frac{1}{2} \left[ (\lambda + 2\mu) \right. \\ & \times \left( \frac{u_+^+ - 2u + u_-^-}{2\Delta^2} - \frac{u^+ - u_- - u_+ + u^-}{2\Delta^2} \right. \\ & + \frac{u_+^+ - 2u + u_+^-}{2\Delta^2} \left. \right) + \mu \left( \frac{u_+^+ - 2u + u_-^-}{2\Delta^2} \right. \\ & + \frac{u^+ - u_- - u_+ + u^-}{2\Delta^2} + \frac{u_+^+ - 2u + u_+^-}{2\Delta^2} \left. \right) \\ & \left. + (\lambda + \mu) \left( \frac{v_+^+ - v_+^- + v_-^+ - v_-^-}{2\Delta^2} \right) \right] = 0 \end{aligned} \quad (\text{A-1})$$

and

$$\begin{aligned} & \rho\omega^2 \left[ bv + \frac{(1-b)}{4}(v^+ + v^- + v_+ + v_-) \right] \\ & + a \left[ (\lambda + 2\mu) \frac{v_+^+ - 2v + v_-^-}{\Delta^2} + \mu \frac{v^+ - 2v + v^-}{\Delta^2} \right. \\ & + (\lambda + \mu) \frac{u_+^+ - u_+^- + u_-^+ - u_-^-}{4\Delta^2} \left. \right] + (1-a) \frac{1}{2} \left[ (\lambda + 2\mu) \right. \\ & \times \left( \frac{v_+^+ - 2v + v_-^-}{2\Delta^2} + \frac{v^+ - v_- - v_+ + v^-}{2\Delta^2} \right. \\ & + \frac{v_+^+ - 2v + v_+^-}{2\Delta^2} \left. \right) + \mu \left( \frac{v_+^+ - 2v + v_-^-}{2\Delta^2} \right. \\ & - \frac{v^+ - v_- - v_+ + v^-}{2\Delta^2} + \frac{v_+^+ - 2v + v_+^-}{2\Delta^2} \left. \right) \\ & \left. + (\lambda + \mu) \left( \frac{u_+^+ - u_+^- + u_-^+ - u_-^-}{2\Delta^2} \right) \right] = 0, \end{aligned} \quad (\text{A-2})$$

where  $\Delta$  is the grid point interval,  $u = u_{m,n}$ ,  $u^+ = u_{m+1,n}$ ,  $u^- = u_{m-1,n}$ ,  $u_+ = u_{m,n+1}$ ,  $u_- = u_{m,n-1}$ ,  $u_+^+ = u_{m+1,n+1}$ ,  $u_-^- = u_{m-1,n-1}$ ,  $u_+^- = u_{m+1,n-1}$ ,  $u_-^+ = u_{m-1,n+1}$  and the equivalent for  $v_{+,-}^{\pm}$ .

By substituting a vector plane-wave solution,

$$\begin{pmatrix} u \\ v \end{pmatrix} = \begin{pmatrix} U \\ V \end{pmatrix} e^{-i\kappa \cdot \mathbf{r}}, \quad (\text{A-3})$$

where  $\kappa = (\kappa_x, \kappa_z)$  is the wave vector and  $\mathbf{r} = (x, z)$  is the position vector, into equations (A-1) and (A-2), one obtains a homogeneous linear system of two equations with two unknowns ( $U$  and  $V$ ). The determinant of this homogeneous system must equal zero, leading to a quadratic equation in  $\omega$  in terms of  $\kappa = |\kappa|$ . The two solutions of this determinant represent the numerical compressional- and shear-wave modes. By using the relations for the phase velocity,  $v_p = \omega/\kappa$ , and the group velocity,  $v_g = \partial\omega/\partial\kappa$ , we obtain the numerical group and phase velocities  $\hat{v}_{pp}$ ,  $\hat{v}_{pg}$ ,  $\hat{v}_{sg}$ , and  $\hat{v}_{ss}$ . Finally, normalized numerical velocities are obtained by dividing by the exact values. The final expressions depend on  $K$  (the wavenumber in grid-point units equal to  $\kappa\Delta/2\pi$  and also equal to the inverse of  $G$ , the number of grid points per wavelength),  $\theta$  (the propagation angle),  $\sigma$  (the Poisson ratio in the homogeneous medium), and  $a$  and  $b$  (the weighting factors of the rotated and lumped mass schemes):

$$\frac{\hat{v}_{pp}}{v_{pp}} = \frac{1}{2\pi K} \sqrt{\frac{\gamma_1 + \sqrt{\gamma_1^2 - 4\gamma_2\alpha_3}}{2\alpha_3}}, \quad (\text{A-4})$$

$$\frac{\hat{v}_{sp}}{v_{sp}} = \frac{1}{R2\pi K} \sqrt{\frac{\gamma_1 - \sqrt{\gamma_1^2 - 4\gamma_2\alpha_3}}{2\alpha_3}}, \quad (\text{A-5})$$

$$\frac{\hat{v}_{pg}}{v_{pg}} = \frac{1}{2\pi} \frac{\partial}{\partial K} \sqrt{\frac{\gamma_1 + \sqrt{\gamma_1^2 - 4\gamma_2\alpha_3}}{2\alpha_3}}, \quad (\text{A-6})$$

and

$$\frac{\hat{v}_{sg}}{v_{sg}} = \frac{1}{R2\pi} \frac{\partial}{\partial K} \sqrt{\frac{\gamma_1 - \sqrt{\gamma_1^2 - 4\gamma_2\alpha_3}}{2\alpha_3}}, \quad (\text{A-7})$$

where

$$\alpha_1 = a[-2 + 2\cos \bar{\kappa}_x] + (1-a)[-1 + \cos \bar{\kappa}_x - \cos \bar{\kappa}_z + \cos \bar{\kappa}_x \cos \bar{\kappa}_z],$$

$$\alpha_2 = a[-2 + 2\cos \bar{\kappa}_z] + (1-a)[-1 - \cos \bar{\kappa}_x + \cos \bar{\kappa}_z + \cos \bar{\kappa}_x \cos \bar{\kappa}_z],$$

$$\alpha_3 = b + \frac{(1-b)}{2}(\cos \bar{\kappa}_x + \cos \bar{\kappa}_z),$$

$$\gamma_1 = \alpha_3(\alpha_1 + \alpha_2)(1 + R^2),$$

and

$$\begin{aligned} \gamma_2 = & (\alpha_1 R^2 + \alpha_2)(\alpha_1 + \alpha_2 R^2) \\ & - (R^4 - 2R^2 + 1)\sin^2 \bar{\kappa}_x \sin^2 \bar{\kappa}_z. \end{aligned}$$

In the computation of these coefficients,  $\bar{\kappa}_x = \kappa\Delta \cos \theta = 2\pi K \cos \theta$  and  $\bar{\kappa}_z = \kappa\Delta \sin \theta = 2\pi K \sin \theta$  are the wave-vector components in grid-point units. The  $v_s/v_p$  ratio,  $R$ , is related to Poisson's ratio,  $\sigma$ , by

$$R^2 = \frac{\mu}{\lambda + 2\mu} = \frac{0.5 - \sigma}{1 - \sigma}. \quad (\text{A-8})$$

## APPENDIX B

## THE INFLUENCE OF THE FINITE DIFFERENCE OPERATOR SIZE

If significant savings are possible with a nine-point star by making use of rotated operators, then it is tempting to seek greater savings by using larger differencing stars, possibly making use of higher order differencing schemes. The use of larger differencing stars carries a computational overhead because the sparsity of the finite-difference matrix is affected. The critical consideration is the RAM storage requirement. It is possible to evaluate the trade-off between the increase in accuracy and the increase in storage requirements for the inclusion of additional grid points in the differencing stars. This trade-off depends on the scheme used to store and solve the matrix equation. There are two principal schemes. The first, and most straightforward, is to order the grid points by row or by column, leading to a banded matrix structure. For a square  $n \times n$  mesh using a nine-point differencing star, this scheme has storage requirements given by

$$M_9 = Cn^3, \quad (\text{B-1})$$

where  $C$  is a constant (e.g., Pratt, 1990).

If, instead, a 13-point differencing star is used (as in Figure 1b) together with a banded matrix structure, then the bandwidth of the matrix will effectively double, leading to storage requirements

$$M_{13} = 2Cn_4^3 \quad (\text{B-2})$$

for a square  $n_4 \times n_4$  mesh ( $C$  is virtually unchanged). If we are to save storage requirements, we will have to obtain a corresponding increase in accuracy such that  $M_{13} \leq M_9$ , or

$$\frac{n_4}{n} \leq \sqrt[3]{\frac{1}{2}} = 0.79. \quad (\text{B-3})$$

Thus, to save storage requirements, the 13-point differencing stars must be accurate enough to allow a 21% reduction in the number of grid points per wavelength. This would seem possible and worth pursuing.

These arguments, however, change when the solution scheme is based on optimal ordering schemes, such as the method of nested dissection (George and Liu, 1981). The savings offered by such a scheme are such that it would be impractical to consider solving large problems in the frequency

domain without nested dissection ordering. In this case the storage requirements are

$$M = C'n^2 \log_2 n + \mathcal{O}(n^2), \quad (\text{B-4})$$

where  $n$  is half the size of the two-way dissector on an  $n \times n$  grid. For a nine-point star, this dissector is of size  $2n$ . If we use a 13-point star on an  $n_4 \times n_4$  grid, the dissector is of size  $4n_4$ . Let us assume the 13-point star allows us to reduce the number of grid points per wavelength such that  $n_4 = kn$ . What must the factor  $k$  be for any savings in storage? If we are to save storage with this scheme,

$$C'4k^2n^2 \log_2 n + \mathcal{O}(n^2) \leq C'n^2 \log_2 n + \mathcal{O}(n^2). \quad (\text{B-5})$$

Ignoring terms of order  $\mathcal{O}(n^2)$  (which, for large problems, are much less significant than the  $n^2 \log n$  terms), we obtain

$$k \leq \frac{1}{2}. \quad (\text{B-6})$$

Note that we have assumed  $C'$  in equation (B-4) is independent of the size of the dissector. In fact, if the calculations are made with the correct factors (Štekl, 1997), the result becomes

$$k \leq 0.445. \quad (\text{B-7})$$

Thus, when we use an optimal storage scheme for the matrix, the 13-point differencing stars must be accurate enough to allow more than a 55% reduction in the number of grid points per wavelength. The analysis changes slightly if the aspect ratio of the model is not 1:1, but the cost of the larger stars still demands approximately a 50% decrease in the number of grid points per wavelength before this is worthwhile. As we have shown, the new scheme we present requires approximately four grid points per wavelength (for less than 5% errors). Since one cannot subsample the wavefield below the Nyquist criterion of two grid points per wavelength, there is no benefit in using a differencing star larger than nine points. [The 5% figure is slightly misleading. In fact, the current scheme could be tuned to smaller errors by limiting the range of  $K$ , the number of gridpoints per wavelength, in the minimization problem (equation [30]), frequency by frequency.]